

Field-tunable toroidal moment in a chiral-lattice magnet

Lei Ding^{1,*}, Xianghan Xu^{2,*}, Harald O. Jeschke³, Xiaojian Bai¹, Erxi Feng¹,
Admasu Solomon Alemayehu², Jaewook Kim², Feiting Huang², Qiang Zhang¹,
Xiixin Ding⁴, Neil Harrison⁴, Vivien Zapf⁴, Daniel Khomskii⁵,
Igor I. Mazin^{6,†}, Sang-Wook Cheong^{2,†}, Huibo Cao^{1,†}

¹*Neutron Scattering Division, Oak Ridge National Laboratory, Oak Ridge, TN 37831, USA*

²*Rutgers Center for Emergent Materials and Department of Physics and Astronomy, Piscataway, NJ 08854, USA*

³*Research Institute for Interdisciplinary Science, Okayama University, Okayama 700-8530, Japan*

⁴*Los Alamos National Laboratory, Los Alamos, New Mexico 87545, USA*

⁵*II. Physikalisches Institut, Universität zu Köln, Zùlpicher Straße 77, D-50937 Köln, Germany*

⁶*Department of Physics and Astronomy, George Mason University, Fairfax, VA 22030, USA*

A toroidal dipole moment appears independent of the electric and magnetic dipole moment in the multipole expansion of electrodynamics. It arises naturally from vortex-like arrangements of spins. Observing and controlling spontaneous long-range orders of toroidal moments are highly promising for spintronics but remain challenging. Here we demonstrate that a vortex-like spin configuration with a staggered arrangement of toroidal moments, a ferritoroidal state, is realized in a chiral triangular-lattice magnet BaCoSiO_4 . Upon applying a magnetic field, we observe multi-stair toroidal transitions correlating directly with metamagnetic transitions. We establish a first-principles microscopic Hamiltonian that explains both the formation of toroidal states and the metamagnetic toroidal transition as a combined effect of the magnetic frustration and the Dzyaloshinskii-Moriya interactions allowed by the crystallographic chirality in BaCoSiO_4 .

*These authors contributed equally to this work.

†Email: imazin2@gmu.edu, sangc@physics.rutgers.edu, caoh@ornl.gov

A toroidal dipole moment differs from electric and magnetic dipoles by breaking both space inversion and time reversal symmetry. In localized spin systems, it can be generated by a head-to-tail arrangement of magnetic moments [1, 2, 3, 4, 5, 6, 7, 8, 9]. A uniform arrangement of toroidal moments leads to the so-called ferrotoroidal order that is of great fundamental interest in condensed matter physics and for potential applications in spintronics [3, 6, 10, 11]. From the symmetry point of view, toroidal moments are conventionally akin to the antisymmetric components in the linear magnetoelectric tensor. Imposed by the symmetry constraint, the switch of toroidal moments remains challenging because of the requirement of a crossed magnetic and electric field in, so far, the well-studied ferrotoroidal materials [12, 13, 14]. By introducing an extra dipole order (magnetic or/and electric), the multiferroic coupling provides an easy way of controlling and mutually tuning of toroidal moments through applying only a magnetic or electric field [4]. A lattice with chirality provides a natural environment for simultaneous existence of multi-dipole orders.

Chirality is a geometrical property, meaning that an object subjected to the spatial inversion cannot be superimposed upon itself by any combination of rotations and translations [15, 16]. Crystallographic chirality has been found to be instrumental in stabilizing unusual magnetic orders such as multiferroicity [17, 18], skyrmion [19, 20, 21], helicity chirality [22, 23] and chiral magnetic soliton lattice [24]. When combined with the magnetic frustration characteristic of antiferromagnetic interactions in equilateral triangles, spins may form a 120° vortex-like configuration [25, 26], as shown in Fig. 1, generating a non-zero toroidal moment breaking both the spatial inversion and time reversal symmetry [25, 26, 27]. Depending on the sense of the in-plane spin rotations, the toroidal moment is either positive (“+”) or negative (“-”). Manipulating toroidal moments directly by a magnetic field is possible in a chiral magnetic vortex, if an out-of-plane spin component is present and coupled with the in-plane spin texture through Dzyaloshinskii-Moriya (DM) interactions [28, 29]. Following this strategy, we find a ferritoroidal order in a unique vortex-like spin configuration in the chiral magnet BaCoSiO₄. By applying a small magnetic field, the toroidal moments are uniformly aligned, thereby leading to a ferri- to ferrotoroidal transition. This toroidal transition, as well as the simultaneously scalar ferri- to ferrochiral transition, is fully explained within a magnetic Hamiltonian accounting for the magnetic frustration and antisymmetric DM interactions. A key property of this Hamiltonian, as derived from first principles calculations, is a rather special and not immediately obvious hierarchy of Heisenberg exchange parameters, which does not correlate with the length of the corresponding Co-Co bonds.

The stuffed tridymite BaCoSiO₄ crystallizes in the polar space group $P6_3$. The crystal structure is *chiral* and adopts only one enantiomorph [30]. Co atoms are tetrahedrally coordinated by oxygen with a large off-center distortion and the nearest Co atoms form spin trimers in the *ab* plane (Fig. S1). Magnetic interactions between Co²⁺ ions are expected to be small due to long and indirect exchange paths through adjacent SiO₄ tetrahedra. The Curie-Weiss law describes well the high-temperature ($150 \lesssim T \lesssim 300$ K) magnetic susceptibility, with a negative Weiss temperatures $\theta_{\text{CW}}^{ab} = -10(2)$ K for $\mathbf{H} \parallel ab$ and $\theta_{\text{CW}}^c = -26.2(4)$ K for $\mathbf{H} \parallel c$. The fitted Curie constants correspond to effective moments $\mu_{\text{eff}}^{ab} = 4.6(4)\mu_{\text{B}}$ and $\mu_{\text{eff}}^c = 4.4(2)\mu_{\text{B}}$, consistent with the high-spin state of Co²⁺ cation with $S = 3/2$ and a nearly isotropic *g*-tensor of ≈ 2.3 (note that this deviates considerably from the nonrelativistic value $g = 2$, indicating sizeable spin-orbit effects).

At low temperatures, the bulk magnetic susceptibility develops an anomaly at $T_N \sim 3.2$ K, attributed to a long-range magnetic order. The isothermal magnetization data of BaCoSiO_4 in the ordered phase are shown in Fig. 2a, and exhibit a sequence of metamagnetic transitions. Starting with a zero-field cooled sample, the first transition to $\sim 0.1\mu_B$ is observed at low fields (≤ 150 Oe) for $\mathbf{H} \parallel c$, stemming from alignment of weak ferromagnetic domains. After a slow and linear ramp, a second transition to $\sim 0.4\mu_B$ occurs at a critical field $\mu_0 H_C \sim 1.2$ T. This corresponds to a spin flip in one of the ferrotoroidal sublattices, as we will elaborate further below. Similar transitions occur with small hysteresis loops for reversed fields. Using pulsed magnetic field, we measured the magnetization up to 60 T along different crystallographic directions [Fig. 2a, inset]. A much higher field is needed to reach saturation with the magnetic field applied along the c axis, which implies the presence of a considerable easy-plane anisotropy in the ab plane, formally not expected for Co^{2+} in a tetrahedral environment, but consistent with $g > 2$. The slope changes around 10 and 40 T before the saturation suggest additional transitions of a completely different nature.

The zero-field magnetic structure of BaCoSiO_4 was determined from powder neutron diffraction experiments. The diffraction pattern at 1.8 K shows a set of satellite reflections that can be indexed with a propagation vector $\mathbf{k} = (1/3, 1/3, 0)$ with respect to the crystallographic unit cell. The thermal evolution of the reflection $(2/3, 2/3, 0)$ confirms the magnetic origin of the satellite reflections [Fig. 2b, inset]. A power-law fit to the integrated intensity as a function of temperature gives a critical exponent $\beta = 0.37(1)$ and $T_N = 3.24(1)$ K. The symmetry analysis [31] and Rietveld refinement [32] yield a complex magnetic structure where the in-plane components of magnetic moments form a vortex-like pattern [Fig. 2d]. The structure is consistent with the magnetic space group $P6_3$ (No.173.129) with a $\sqrt{3} \times \sqrt{3}$ magnetic supercell. To test the reliability of the refined in-plane spin orientation, we evaluate the profile factor R_p of the fit as a function of uniform rotation (ϕ) of spins within the ab plane. Fig. 2b reveals clear minimums at $\phi \sim 0^\circ$ (the structure in Fig. 2d) and $\phi \sim 120^\circ$, indicating the global orientation of the spin structure with respect to the lattice is strongly constrained. The bulk magnetization data imply the existence of a weak ferromagnetic canting along the c axis, which is allowed by the magnetic space group symmetry, however it can not be unequivocally determined from current neutron data. A satisfactory fit can be achieved by setting canting angles to zero, yielding an ordered moment $m_{\text{Co}}(0\text{T}) = 2.71(5) \mu_B$ at 1.8 K and $\sim 3.67 \mu_B$ at zero temperature from extrapolating the power law fitting [Fig. S2a]. To appreciate the toroidal nature of the magnetic ground in BaCoSiO_4 , it is instructive to decompose the structure into three interpenetrating sublattices (red, cyan and blue) [Fig. 2d], each of which is a network of trimers (up- and down-triangles). Spins on every trimer form a 120° configuration that resembles a vortex and generates a non-zero toroidal moment. All trimers belonging to a single sublattice have the identical toroidal moment, giving rise to three ferrotoroidal sublattices. In zero field, two of them (red and blue) have the same total moment \mathbf{t} , while the remaining one (cyan) has the opposite moment, leading to a net moment of $-\mathbf{t}$ or $+\mathbf{t}$ within a macroscopic magnetic domain. We dub this structure *ferritoroidal*.

The field response of the magnetic ground state in BaCoSiO_4 is investigated using single-crystal neutron diffraction. Fig. 2c shows the integrated intensity of the magnetic reflection $(2/3, 2/3, 0)$ and the nuclear reflection $(-1, 1, 0)$ as a function of magnetic field along the c axis at 1.5 K. The former is increasingly suppressed by fields and eventually

disappears at $\mu_0 H_C \sim 1.2$ T while the latter gains significant extra intensity, indicating a field-induced transition to a $\mathbf{k} = \mathbf{0}$ magnetic structure. The refined $\mathbf{k} = \mathbf{0}$ magnetic structure has the same magnetic space group symmetry as the zero-field structure. The key difference is that the sublattice (cyan) with the opposite toroidal moment is flipped by 180° in field, yielding a uniformly aligned toroidal moment for all three sublattices with a total toroidal moment $+3\mathbf{t}$ [Fig. 2e], termed *ferrotoroidal*. This remarkable field-induced ferri- to ferrotoroidal transition directly correlates with the metamagnetic transition observed in the bulk magnetization measurements at the same critical field.

While the magnetic patterns, at first glance, seem nearly incomprehensibly complicated, it actually has a straightforward microscopic explanation. To show that, we first calculated the isotropic Heisenberg magnetic interactions using the density functional theory (DFT). Inspecting the Co t_{2g} bands crossing the Fermi level, we found that the five shortest Co-Co bonds, with $d_{\text{Co-Co}}$ between 5.11 and 5.41 Å, all have hopping integrals of roughly the same order [Fig. S3] so they should be included in the minimal model [Fig. 3a]. Next, we performed total energy calculations for selected spin configurations and determined exchange parameters J by fitting the results to the mean field energies of a Heisenberg model. Fig. 3b shows the fitted model parameters as a function of onsite interaction U , using the room-temperature crystal structure as input in DFT calculations. All five exchange couplings are antiferromagnetic. Most interestingly, despite all bond lengths being similar, two interactions stand out as dominant, independent of U : the intra-layer coupling J_t and the inter-layer coupling J_z . The Co atoms connected by these two bonds form the three interpenetrating sublattices shown in Fig. 2d. Within each sublattice, we expect that frustrated J_t interactions impose 120° spin configurations on trimers that are antiferromagnetically coupled by J_z . This explains the major part of the experimentally determined magnetic structure. In addition, relativistic DFT calculations indicate a strong easy-plane single-ion anisotropy (~ 2 K, comparable to the dominant exchange interactions). This is nontrivial, since Co^{2+} in a tetrahedral environment features a full e_g shell and half-filled t_{2g} , and formally is not supposed to have a sizeable orbital moments. The key is that the CoO_4 tetrahedra are considerably distorted and moreover Co^{2+} is strongly off-centered (Fig. 3a), so that the e_g and t_{2g} orbitals are actually mixed. This is also consistent with the pulsed-field magnetization measurements.

Of the three sublattices in Fig. 2d one (cyan) has its toroidal moment opposite to the others. This results from the subleading exchange interactions $\{J'_t, J''_t, J_c\}$ [Fig. 3a]. The first two connect the trimers within the ab plane, while the last one connects those along the c axis. A close inspection of the lattice connectivity reveals that all three subleading interactions with the help of J_t form various triangular units. The total energy associated with subleading interactions is the lowest if spins on all these triangular units have 120° arrangements (neglecting the weak ferromagnetic canting). Yet, this condition cannot be satisfied. Fig. 3d colors all “frustrated” triangles that do *not* have 120° configurations in a ferri- and ferrotoroidal state. We see clear switching of colored triangles from one state to another, indicating a direct competition between the intra-layer J'_t and J''_t couplings and the inter-layer J_c couplings. In BaCoSiO_4 , this competition favors a ferritoroidal state by a small margin of energy in zero field.

However, this Heisenberg model, with (or without) the single-ion anisotropy, is insufficient in explaining the weak ferromagnetic canting and the spin-space anisotropy evidenced from our experimental data. To this end, we introduce

the antisymmetric Dzyaloshinskii-Moriya (DM) interactions [27, 28, 29] within the structural trimers [Fig. 3a]. All three components of a DM vector on a nearest neighbor bond are allowed due to lack of symmetry constraints. It is rather difficult to calculate the DMI from the first principles, so for the moment we are assuming that all three components are present. The DM vectors on different bonds of the trimer are related by the 3-fold rotations. Assuming a uniform canting along c and 120° configurations in the ab plane for a trimer, the out-of-plane DM component $D_z \hat{z}$ contributes $-\frac{3\sqrt{3}}{2}|D_z|S_{xy}^2$ in energy, where S_{xy} is the length of in-plane spin component. Therefore, this term always favors coplanar spin configurations instead of canting. Taking into account that the 120° configuration has a 3-fold vortex symmetry, we find that the energy associated with the in-plane DM component, \mathbf{D}_{xy} , is $3\sqrt{3}(\mathbf{D}_{xy} \cdot \mathbf{S}_{xy})(\mathbf{S}_z \cdot \hat{z})$, where \mathbf{S}_z is the out-of-plane spin component. There are two important ramifications. First, the two components of spins are locked together, namely if \mathbf{S}_z flips, so does \mathbf{S}_{xy} as well, to keep the DM energy gain. This is actually the essential physical factor which couples the net component of magnetization M_z to the toroidal moment and allows to control toroidal moments by altering M_z , e.g., by external fields. Second, to minimize the DM energy for a fixed spin canting, \mathbf{S}_{xy} has to be anti-parallel to \mathbf{D}_{xy} if $\mathbf{S}_z \parallel \hat{z}$ or parallel to \mathbf{D}_{xy} if $\mathbf{S}_z \parallel -\hat{z}$, which means that we can read off the direction of the DM vector directly from the experimental spin structure, assuming $D_z = 0$. In Fig. 3c, we show by green arrows the total DM vector for each bond, which is the vector sum of D_\perp and D_\parallel components and makes a $\sim 30^\circ$ angle with the bond, as determined from the magnetic structure. For each sublattice connected by J_t and J_z bonds, the DM interaction creates a uniform c axis canting and corresponding in-plane toroidal spin texture. However, different sublattices are independent of each other, hence ferri- and ferrotoroidal states would have had the same energy, if not for the subleading Heisenberg interactions $\{J'_t, J''_t, J_c\}$.

We now fully understand the metamagnetic ferrotoroidal transition. Indeed, because of the DMI-induced ferromagnetic canting, the small $\{J'_t, J''_t, J_c\}$ -driven energy gain associated with the ferrotoroidal arrangement competes directly with the Zeeman interaction favoring the ferrotoroidal phase. This leads to the spin-flip (also a toroidal flip) manifested through the sudden increase of magnetization along the c axis by a factor of three at the metamagnetic transition [Fig. 2e]. A direct numerical calculation of magnetization using the complete model with all interactions discussed thus far is given in Fig. 2a and shows good agreement with the data. See Supplementary Information and Method section for more details and model parameters.

At a fundamental level, the physics emerging in BaCoSiO_4 originates from its chiral crystal structure. For a single triangle in 3 dimensions, there is a set of three mirror planes perpendicular to the triangle and one extra mirror plane containing the triangle. The former allows both D_z and D_\perp components of the DM interaction, while the latter allows only D_z . When D_\perp is absent, D_z with the correct sign could create a vortex configuration, however the ferromagnetic canting is unfavored in this case. Thus, the intimate coupling between magnetization and toroidal moment is lost. In BaCoSiO_4 , the triangles are decorated by distorted CoO_4 tetrahedra which break all the mirror planes while still preserving the 3-fold symmetry. The D_\parallel term is then allowed, and plays an essential role in generating chiral vortex structures wherein the c axis canting is coupled with the sense of the spin rotation in the ab plane. A direct control of toroidal moments

using only magnetic fields is therefore possible through controlling the bulk magnetization by a uniform magnetic field, instead of using a conjugate field such as the curl of magnetic fields. The same arguments show that at this transition the scalar chirality κ (Fig. 1), existing in Co triangles, also changes from the ferrichiral to ferrochiral state, similar to the three-sublattice description for the toroidal transition. The ferrochiral state with a noncoplanar spin configuration acquires the considerable Berry curvature which can lead to a variety of exotic physical phenomena such as topological magnon excitations [33, 34].

In summary, we studied a rare chiral triangular-lattice magnet BaCoSiO_4 through bulk magnetization measurements and neutron diffraction experiments. We uncovered a novel vortex-like spin texture and a magnetic-field-induced ferri- to ferrotoroidal transition for the first time. Combining *ab initio* density functional theory calculations and theoretical modeling, we have derived the microscopic energy balance and were able to explain quantitatively the complex magnetic structure and the field-induced metamagnetic/toroidal phase transition, neither of which had been observed before in any compound. Our work shows that BaCoSiO_4 is an excellent platform to study field-tunable toroidal moments and to explore their interplay with the structural and magnetic chirality. Further studies on the magnetoelectric effects and dynamical responses of toroidal spin textures are liable to bring up further new physics and potential applications.

Chiral configuration	Left		mirror	Right	
Toroidal moment, \mathbf{t}	—	+		+	—
Vector chirality, ϵ	+	+		+	+
Scalar chirality, κ	+	—		+	—

Figure 1: **Toroidal moment and magnetic chirality of spin vortex configurations with 3-fold rotation symmetry.** Four chiral non-coplanar structures are divided into groups of two left-handed ones and two right-handed ones. Those within each group are connected by 2-fold rotations and those between two groups by a mirror operation. The spins (axial vector) are represented as arrows. The dashed line with an ellipsoid indicates one of the three 2-fold axes. Three relevant physical quantities are defined with spins $\{\mathbf{S}_i = 1, 2, 3\}$ numbered anticlockwise: toroidal moment $\mathbf{t} = \sum_i \mathbf{r}_i \times \mathbf{S}_i$ where \mathbf{r}_i is the vector from the center of the triangle to spin \mathbf{S}_i ; vector chirality $\epsilon = \mathbf{S}_1 \times \mathbf{S}_2 + \mathbf{S}_2 \times \mathbf{S}_3 + \mathbf{S}_3 \times \mathbf{S}_1$; scalar chirality $\kappa = (\mathbf{S}_1 \times \mathbf{S}_2) \cdot \mathbf{S}_3$. Green symbols + and — for toroidal moment and vector chirality denote the direction of these quantities with respect to the net magnetic moment, + for parallel and — for anti-parallel. The magnetic vector chirality characterizes the sense of spin rotation along an oriented loop (or line), while the toroidal moment is associated with that around a center. Scalar spin chirality is a measure of non-coplanarity which does not necessarily have a sense of rotation. In the current example, toroidal moment and scalar chirality have a one-to-one correspondence to the net magnetic moment for a given handedness, since all of them are odd under time reversal. In a crystalline material with these chiral spin trimers as basic units, a ferro alignment of net magnetic moments of trimers will lead to a ferro ordering of toroidal moments and scalar chirality.

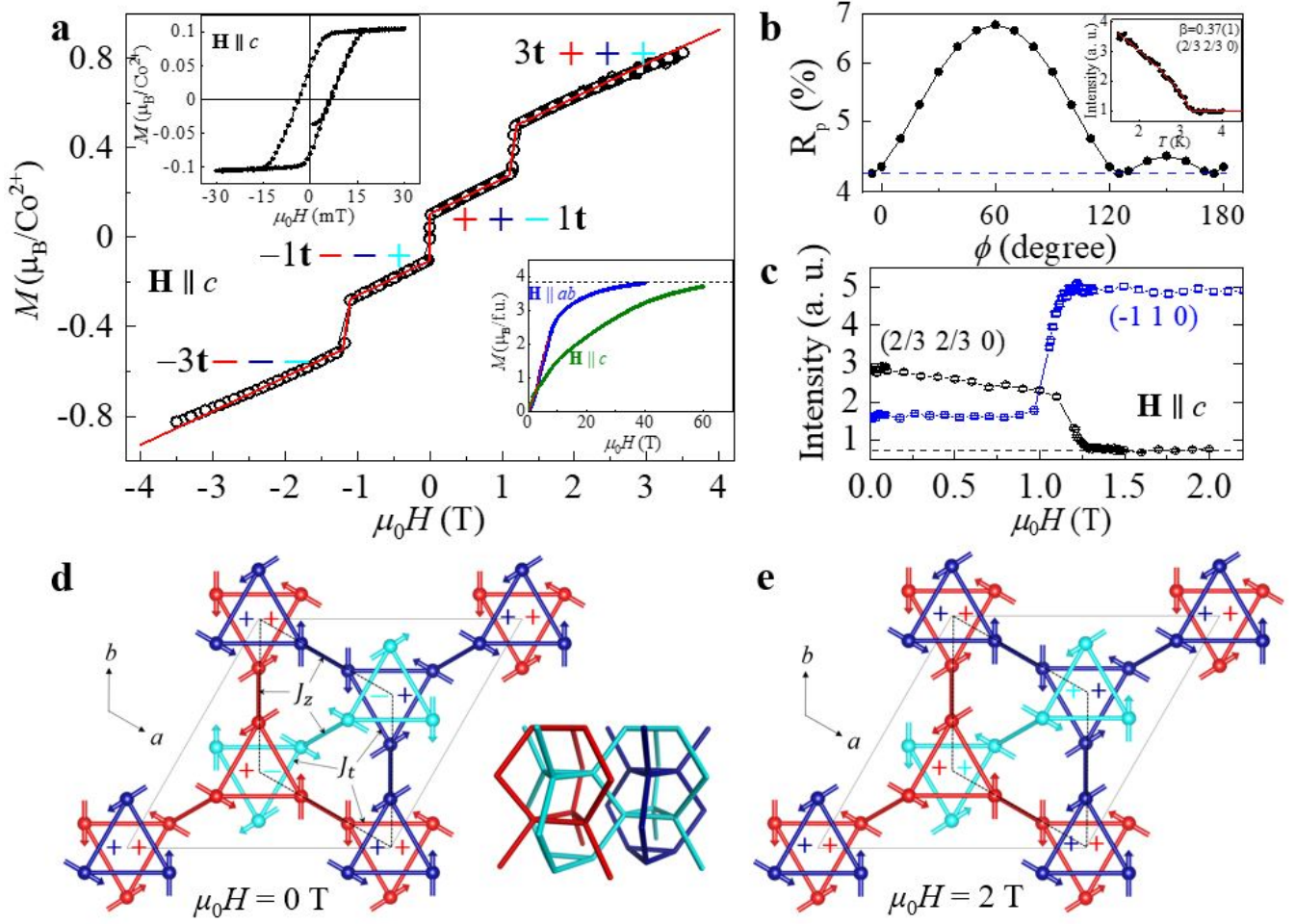


Figure 2: **Zero-field magnetic structure and field-induced ferri- to ferrotoroidal transition in BaCoSiO₄.** **a**, The isothermal bulk magnetization data (open circles) measured at 2 K with the field parallel to the *c* axis and the theoretical calculations (red line) from the full spin Hamiltonian, showing a good agreement between data and calculations. The magnetization up to 60 T in a pulsed magnetic field at 1.5 K is shown in the lower inset, and the magnetization hysteresis at low fields in the upper inset. See caption of panel **d** for the meaning of symbols + and -. **b**, The refined agreement factor for the powder neutron diffraction data as a function of uniform rotation in the *ab* plane. The dashed line marks the best refinement. Inset shows the integrated intensity of the magnetic reflection (2/3 2/3 0) as a function of temperature with an order parameter fit $\sim (1 - T/T_N)^{2\beta}$ (solid line), where β is the critical exponent. **c**, The integrated intensities of reflection (2/3 2/3 0) and (-1 1 0) as a function of magnetic field with $\mathbf{H} \parallel c$ at 1.5 K. **d**, Zero-field magnetic structure of BaCoSiO₄ in a $\sqrt{3} \times \sqrt{3}$ supercell solved from powder neutron diffraction data, showing three interpenetrating ferrotoroidal sublattices (red, blue and cyan) formed by the dominant exchange interactions J_t (intra-layer) and J_z (inter-layer). The direction of toroidal moment for each sublattice is denoted + if it is parallel to the *c* axis and - if anti-parallel. The red and blue sublattices have the same toroidal moment, while the cyan has the opposite moment, leading to a ferritoroidal state with a total moment +1t. The primitive crystallographic unit cell is indicated by the dotted lines. **e**, Magnetic structure of BaCoSiO₄ at 2 T solved from single-crystal neutron diffraction data. All spins on the cyan sublattice are reversed, leading to a ferrotoroidal state with a total toroidal moment +3t. Triangles in panels **d** and **e** lie in two adjacent layers which are bridged by the inter-layer interaction J_z .

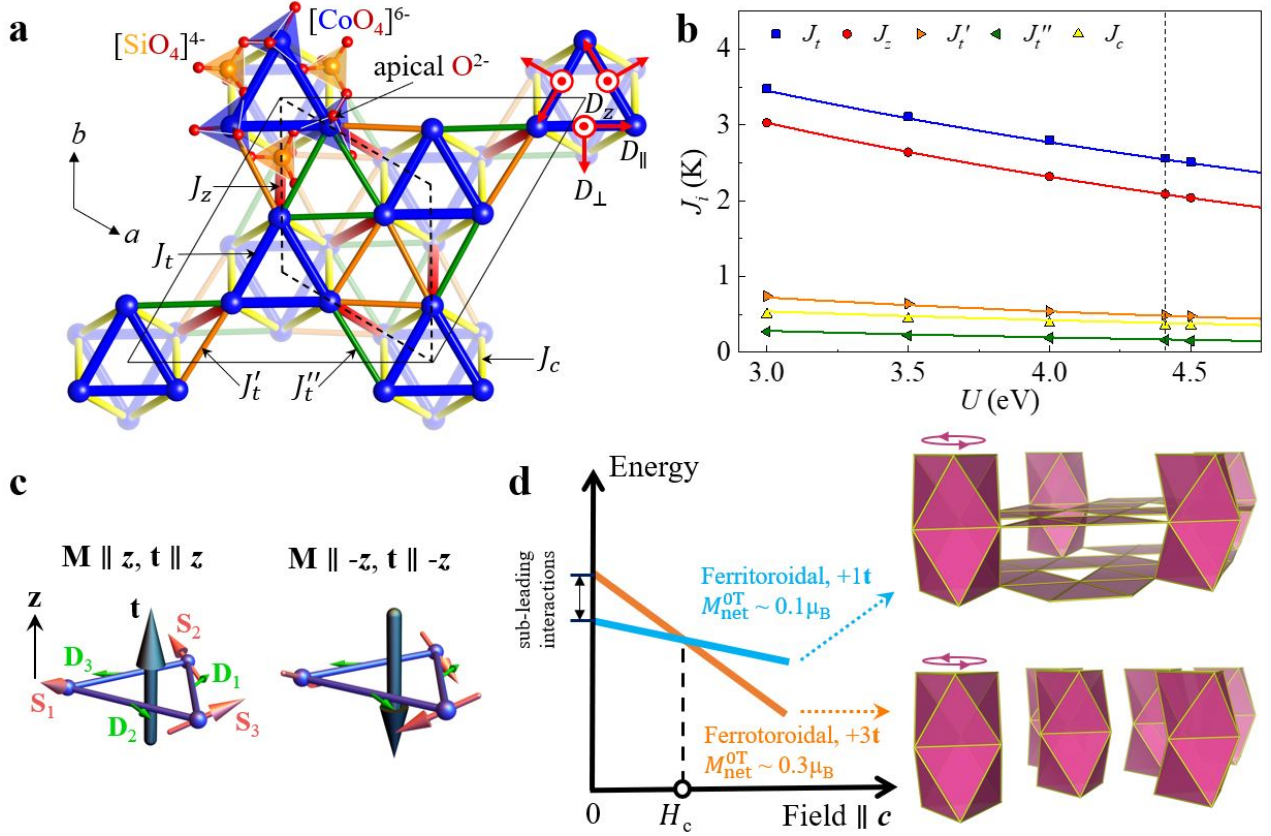


Figure 3: Microscopic magnetic model and the underlying mechanism for the ferritoroidal to ferrotoroidal transition. **a**, Magnetic exchange pathways of BaCoSiO₄, showing three intra-layer couplings $\{J_t, J'_t, J''_t\}$ and two inter-layer couplings $\{J_z, J_c\}$. Three components of a DM vector on the nearest neighbor J_t bonds are indicated by red arrows in a local reference frame. **b**, Density functional theory calculation of exchange interaction strengths as a function of onsite interaction U . The dashed line marks the set of couplings with $U = 4.41$ eV that matches the Weiss temperature from the magnetic susceptibility [Table S2]. **c**, Minimal energy configurations for three spins $\{\mathbf{S}_i, i = 1, 2, 3\}$ on a triangle with an antiferromagnetic Heisenberg interaction and an in-plane DM interaction. The DM vectors $\{\mathbf{D}_i, i = 1, 2, 3\}$ (green arrows) are related by 3-fold rotation symmetry and have the same sense of rotation as the tilting of apical oxygens shown in panel **a**. Each vector makes a $\sim 30^\circ$ angle with the bond, see main text for details. For this set of DM vectors, the resulting spin structure (pink arrows) generates a toroidal moment \mathbf{t} (black arrows) that is always parallel to the magnetization \mathbf{M} . **d**, Energy balance between the ferri- to ferrotoroidal state in magnetic fields. The “frustrated” triangular units that do *not* have 120° configurations (and cost more energy) are highlighted in pink for both states. The ferrotoroidal state has less colored triangles in the ab plane, therefore it is energetically favored by the interactions $\{J'_t, J''_t\}$, similarly the ferritoroidal state is favored by the interaction J_c . Competition between these subleading interactions results in the ferritoroidal structure with a lower energy in zero field. The transition to the ferrotoroidal state occurs when the energy difference is compensated by the Zeeman energy in magnetic fields.

References

- [1] Gorbatshevich, A. A. & Kopaev, Y. V. Toroidal order in crystals. *Ferroelectrics* **161**, 321–334 (1994).
- [2] Ederer, C. & Spaldin, N. A. Towards a microscopic theory of toroidal moments in bulk periodic crystals. *Phys. Rev. B* **76**, 214404 (2007).
- [3] Spaldin, N. A., Fiebig, M. & Mostovoy, M. The toroidal moment in condensed-matter physics and its relation to the magnetoelectric effect. *J. Phys.: Condens. Matter* **20**, 434203 (2008).
- [4] Schmid, H. Some symmetry aspects of ferroics and single phase multiferroics. *J. Phys.: Condens. Matter* **20**, 434201 (2008).
- [5] Van Aken, B., Rivera, J.-P., Schmid, H. & Fiebig, M. Observation of ferrotoroidic domains. *Nature* **449**, 702–705 (2007).
- [6] Cheong, S. W. & Mostovoy, M. Multiferroics: a magnetic twist for ferroelectricity. *Nat. Mater.* **6**, 13–20 (2007).
- [7] Ginzburg, V. L., Gorbatshevich, A. A., Kopayev, Y. V. & Volkov, B. A. On the problem of superdiamagnetism. *Solid State Commun.* **50**, 339–343 (1984).
- [8] Dubovik, V. M. & Tugushev, V. V. Toroid moments in electrodynamics and solid-state physics. *Phys. Rep.* **187**, 145–202 (1990).
- [9] Foggetti, F., Cheong, S.-W. & Artyukhin, S. Magnetic monopoles and toroidal moments in LuFeO_3 and related compounds. *Phys. Rev. B* **100**, 180408 (2019).
- [10] Fiebig, M., Lottermoser, T., Meier, D. & Trassin, M. The evolution of multiferroics. *Nat. Rev. Mater.* **1**, 1–14 (2016).
- [11] Cheong, S. W., Talbayev, D., Kiryukhin, V. & Saxena, A. Broken symmetries, non-reciprocity, and multiferroicity. *npj Quantum Mater.* **3**, 19 (2018).
- [12] Ressouche, E. *et al.* Magnetoelectric MnPS_3 as a candidate for ferrotoroidicity. *Phys. Rev. B* **82**, 100408(R) (2010).
- [13] Zimmermann, A. S., Meier, D. & Fiebig, M. Ferroic nature of magnetic toroidal order. *Nat. Commun.* **5**, 4796 (2014).
- [14] Baum, M. *et al.* Controlling toroidal moments by crossed electric and magnetic fields. *Phys. Rev. B* **88**, 024414 (2013).
- [15] Flack, H. D. Chiral and achiral crystal structures. *Helvetica Chimica Acta* **86**, 905–921 (2003).
- [16] Simonet, V., Loire, M. & Ballou, R. Magnetic chirality as probed by neutron scattering. *Eur. Phys. J. Special Topics* **213**, 5–36 (2012).

- [17] Johnson, R. D. *et al.* MnSb₂O₆: A polar magnet with a chiral crystal structure. *Phys. Rev. Lett.* **111**, 017202 (2013).
- [18] Kinoshita, M. *et al.* Magnetic reversal of electric polarization with fixed chirality of magnetic structure in a chiral-lattice helimagnet MnSb₂O₆. *Phys. Rev. Lett.* **117**, 047201 (2016).
- [19] Muhlbauer, S. *et al.* Skyrmion lattice in a chiral magnet. *Science* **323**, 915–919 (2009).
- [20] Yu, X. Z. *et al.* Real-space observation of a two-dimensional skyrmion crystal. *Nature* **465**, 901–904 (2010).
- [21] Seki, S., Yu, X. Z., Ishiwata, S. & Tokura, Y. Observation of skyrmions in a multiferroic material. *Science* **336**, 198–201 (2012).
- [22] Marty, K. *et al.* Single domain magnetic helicity and triangular chirality in structurally enantiopure Ba₃NbFe₃Si₂O₁₄. *Phys. Rev. Lett.* **101**, 247201 (2008).
- [23] Loire, M. *et al.* Parity-broken chiral spin dynamics in Ba₃NbFe₃Si₂O₁₄. *Phys. Rev. Lett.* **106**, 207201 (2011).
- [24] Togawa, Y. *et al.* Chiral magnetic soliton lattice on a chiral helimagnet. *Phys. Rev. Lett.* **108**, 107202 (2012).
- [25] Sachdev, S. Kagomé and triangular-lattice Heisenberg antiferromagnets: Ordering from quantum fluctuations and quantum-disordered ground states with unconfined bosonic spinons. *Phys. Rev. B* **45**, 12377–12396 (1992).
- [26] Chubukov, A. Order from disorder in a kagomé antiferromagnet. *Phys. Rev. Lett.* **69**, 832–835 (1992).
- [27] Batista, C. D., Lin, S. Z., Hayami, S. & Kamiya, Y. Frustration and chiral orderings in correlated electron systems. *Rep. Prog. Phys.* **79**, 084504 (2016).
- [28] Dzyaloshinsky, I. A thermodynamic theory of weak ferromagnetism of antiferromagnetics. *J. Phys. Chem. Solids* **4**, 241–255 (1958).
- [29] Moriya, T. Anisotropic superexchange interaction and weak ferromagnetism. *Phys. Rev.* **120**, 91–98 (1960).
- [30] Liu, B. & Barbier, J. Structure of the stuffed tridymite derivatives, BaMSiO₄ (*M* = Co, Zn, Mg). *J. Solid State Chem.* **102**, 115–125 (1993).
- [31] Perez-Mato, J. M. *et al.* Symmetry-based computational tools for magnetic crystallography. *Annu. Rev. Mater. Res.* **45**, 217–248 (2015).
- [32] Rodríguez-Carvajal, J. Recent advances in magnetic structure determination by neutron powder diffraction. *Physica B: Condens. Matter* **192**, 55–69 (1993).
- [33] Katsura, H., Nagaosa, N. & Lee, P. A. Theory of the thermal Hall effect in quantum magnets. *Phys. Rev. Lett.* **104**, 066403 (2010).

- [34] Onose, Y. *et al.* Observation of the magnon Hall effect. *Science* **329**, 297–299 (2010).
- [35] Detwiler, J. A. *et al.* Magnetization of UBe_{13} to 60 T. *Phys. Rev. B* **61**, 402–404 (2000).
- [36] Chakoumakos, B. C. *et al.* Four-circle single-crystal neutron diffractometer at the high flux isotope reactor. *J. Appl. Crystallogr.* **44**, 655–658 (2011).
- [37] Cao, H. B. *et al.* DEMAND, a dimensional extreme magnetic neutron diffractometer at the high flux isotope reactor. *Crystals* **9**, 5 (2019).
- [38] Koepnick, K. & Eschrig, H. Full-potential nonorthogonal local-orbital minimum-basis band-structure scheme. *Phys. Rev. B* **59**, 1743–1757 (1999).
- [39] Perdew, J. P., Burke, K. & Ernzerhof, M. Generalized gradient approximation made simple. *Phys. Rev. Lett.* **77**, 3865–3868 (1996).
- [40] Liechtenstein, A. I., Anisimov, V. I. & Zaanen, J. Density-functional theory and strong interactions: Orbital ordering in Mott-Hubbard insulators. *Phys. Rev. B* **52**, R5467–R5470 (1995).
- [41] Mizokawa, T. & Fujimori, A. Electronic structure and orbital ordering in perovskite-type 3d transition-metal oxides studied by Hartree-Fock band-structure calculations. *Phys. Rev. B* **54**, 5368–5380 (1996).
- [42] Ghosh, P. *et al.* Breathing chromium spinels: a showcase for a variety of pyrochlore heisenberg hamiltonians. *npj Quantum Mater.* **4**, 63 (2019).

Methods

Sample preparation and characterization. Powder sample of BaCoSiO_4 was prepared by direct solid-state reaction from stoichiometric mixtures of BaCO_3 , Co_3O_4 and SiO_2 powders all from (Alfa Aesar, 99.99%) as previously reported [30]. The mixture was calcined at 900 °C in air for 12 hours and then re-grounded, pelletized and heated at 1200 °C for 20 h and at 1250 °C for 15 h with intermediate grindings to ensure a total reaction. The resulting powder sample is fine and bright blue in color. Large single crystals were grown using a laser-diode heated floating zone technique. The optimal growth conditions were growth speed of 2-4 mm/h, atmospheric air flow of 0.1 L min⁻¹ and counter-rotation of the feed and seed rods at 15 and 30 rpm, respectively.

Magnetization measurement. Temperature dependence of magnetization $M(T)$ was measured under a field of 0.1 T in a commercial magnetic property measurement system (MPMS-XL7, Quantum Design). Magnetic hysteresis loops with the field along the a and c axes were measured at 2 K. Magnetization up to 60 T was measured by an induction magnetometry technique [35] using a capacitor-bank-driven pulsed magnet at the National High Magnetic Field Laboratory pulsed-field facility at Los Alamos. The pulsed-field magnetization values are calibrated against measurements in a 7 T dc magnet using a superconducting quantum interference device magnetometer (MPMS-XL7, Quantum Design).

Neutron diffraction. Neutron powder diffraction (NPD) experiments were performed on the time-of-flight (TOF) powder diffractometer POWGEN at the Spallation Neutron Source (SNS) at Oak Ridge National Laboratory (ORNL). A powder sample of ~ 2 g was loaded in a vanadium cylinder can and measured in the temperature range of 1.8-10 K with neutron wavelength band centered at $\lambda = 1.5 \text{ \AA}$ and 2.665 \AA , covering the d -space range 0.5-9.0 and 1.1-15.4 \AA , respectively. Single crystal neutron diffraction experiments were carried out on the single crystal neutron diffractometer HB-3A DEMAND equipped with a 2D detector at the High Flux Isotope Reactor (HFIR), ORNL. The measurement used the neutron wavelength of 1.553 \AA selected by a bent perfect Si-220 monochromator [36, 37]. The single crystal (~ 0.2 g) was mounted in a vertical field superconducting cryomagnet with magnetic field up to 5.5 T and measured over the temperature range of 1.5-10 K with magnetic field applied along the c axis. The data refinements were performed by FULLPROF SUITE program [32].

Spin-polarized Density Functional Theory calculations. Electronic structure calculations were performed using the full potential local orbital (fplo) basis [38] and generalized gradient approximation exchange and correlation functional [39]. The crystal structure from Ref. [30] was used. We correct for the strong electronic correlations on Co $3d$ orbitals using a DFT+U method [40] with a fixed value of the Hund's rule coupling $J_H = 0.84$ eV as suggested in Ref. [41]. The Heisenberg Hamiltonian parameters were determined by an energy mapping technique [42].

Full spin model calculations. The experimental magnetization data shown in Fig. 2a was modeled using a full spin Hamil-

tonian, including exchange interactions, single-ion anisotropy and external fields, $\mathcal{H} = \frac{1}{2} \sum_{ij} J_{ij} \mathbf{S}_i \cdot \mathbf{S}_j + A \sum_i (S_i^z)^2 - g\mu_B\mu_0 \sum_i \mathbf{H} \cdot \mathbf{S}_i$ with $g = 2$ and $S = 3/2$. Starting with the Heisenberg interactions strengths produced by DFT calculations, by trial and error, we found following set of parameters reasonably reproducing the experimental magnetization data, $J_t = 2.22$ K, $J_z = 1.87$ K, $J'_t = 0.21$ K, $J''_t = 0.61$ K, $J_c = 0.48$ K, $D_{\parallel} = 1.71$ K, $D_{\perp} = D_{\parallel}/\sqrt{3}$, $D_z = 0$ K and $A = 7.5$ K. Direct numerical minimization of the classical energy was performed for this model using a $\sqrt{3} \times \sqrt{3}$ supercell. The magnetization is obtained by averaging all spins of the lowest energy configuration at each field value, shown as the red line in Fig. 2a.

Acknowledgments

The work at Oak Ridge National Laboratory (ORNL) was supported by the U.S. Department of Energy (DOE), Office of Science, Office of Basic Energy Sciences, Early Career Research Program Award KC0402010, under Contract DE-AC05-00OR22725. This research used resources at the High Flux Isotope Reactor and the Spallation Neutron Source, the DOE Office of Science User Facility operated by ORNL. The work at Rutgers University was supported by the DOE under Grant No. DOE: DE-FG02-07ER46382. The work of D. Kh. was funded by the Deutsche Forschungsgemeinschaft (DFG, German Research Foundation) - Project number 277146847 - CRC 1238. I.I.M. acknowledges support from DOE under Grant No. DE-SC0021089. The National High Magnetic Field Laboratory is funded by the U.S. National Science Foundation through Cooperative Grant No. DMR-1157490, the U.S. DOE and the State of Florida.

Author contributions

S.-W.C. conceived the BaCoSiO₄ project. H.B.C., S.-W.C. and I.I.M. supervised this work. X.X. and A.S.A. grew the sample. X.X., J.K., F.H., X.D., N.H., V.Z. and S.-W.C. measured bulk magnetization data. L.D., E.F., Q.Z., and H.B.C. performed neutron diffraction experiments and data analysis. H.O.J., X.B., D.K. and I.I.M. performed DFT calculations and theoretical modeling. L.D., X.B., I.I.M., S.-W.C. and H.B.C. wrote the paper with comments from all the authors.

Competing financial interests

The authors declare no competing financial interests.

Field-tunable toroidal moment in a chiral-lattice magnet

Supplementary Information

Lei Ding^{1,*}, Xianghan Xu^{2,*}, Harald O. Jeschke³, Xiaojian Bai¹, Erxi Feng¹,
Admasu Solomon Alemayehu², Jaewook Kim², Feiting Huang², Qiang Zhang¹,
Xiixin Ding⁴, Neil Harrison⁴, Vivien Zapf⁴, Daniel Khomskii⁵,
Igor I. Mazin^{6,†}, Sang-Wook Cheong^{2,†}, Huibo Cao^{1,†}

¹*Neutron Scattering Division, Oak Ridge National Laboratory, Oak Ridge, TN 37831, USA*

²*Rutgers Center for Emergent Materials and Department of Physics and Astronomy, Piscataway, NJ 08854, USA*

³*Research Institute for Interdisciplinary Science, Okayama University, Okayama 700-8530, Japan*

⁴*Los Alamos National Laboratory, Los Alamos, New Mexico 87545, USA*

⁵*II. Physikalisches Institut, Universität zu Köln, Zùlpicher Straße 77, D-50937 Köln, Germany*

⁶*Department of Physics and Astronomy, George Mason University, Fairfax, VA 22030, USA*

Contents

S.1 Crystal structure and magnetic structure determination of BaCoSiO₄	2
S.2 Magnetization characterization	4
S.3 Density functional theory calculations	5
S.4 Theoretical modeling	8

*These authors contributed equally to this work.

†Email: imazin2@gmu.edu, sangc@physics.rutgers.edu, caoh@ornl.gov

S.1 Crystal structure and magnetic structure determination of BaCoSiO₄

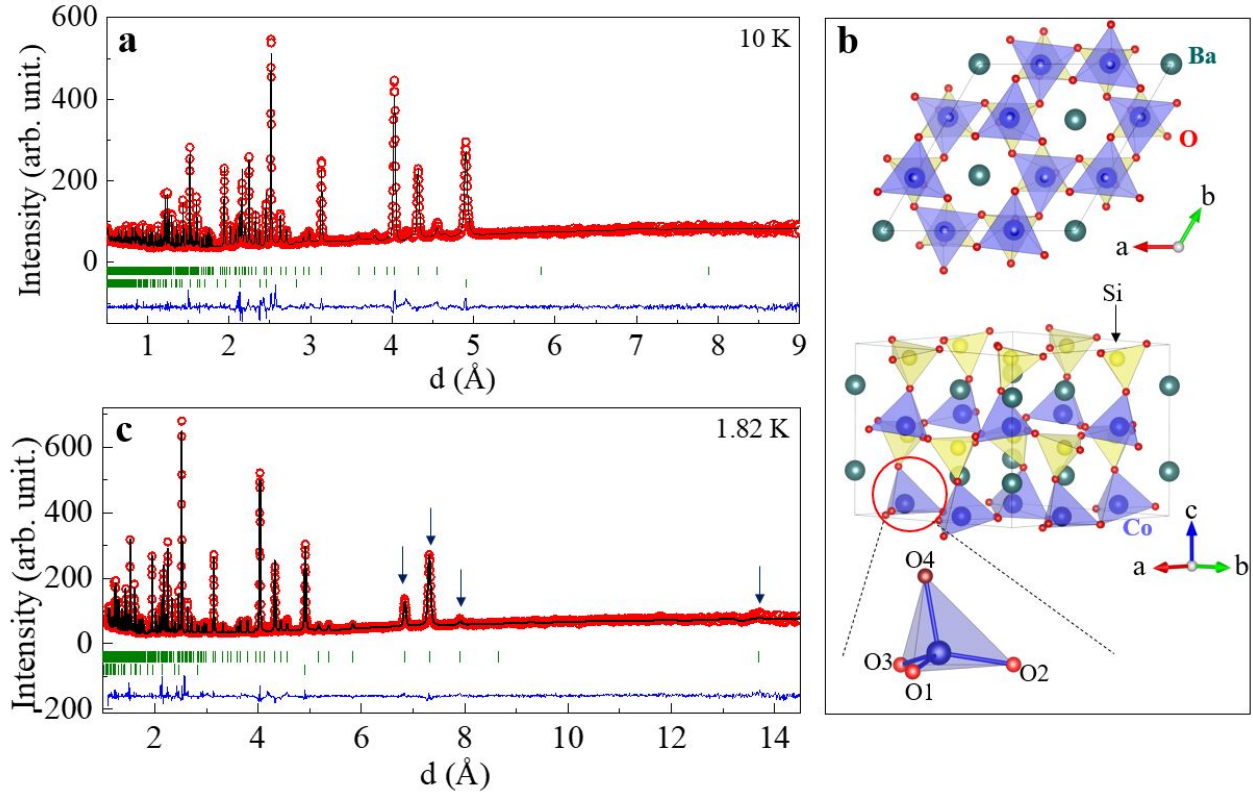


Figure S1: **a**, Rietveld refinement of neutron diffraction data collected at 10 K. Open red circles and solid black line represent experimental and calculated intensities, respectively. Solid blue line at the bottom of the panel shows the difference between them. The upper green tick marks stand for the positions of the Bragg reflections while the lower marks denote the impurity phase CoO₃ (weight fraction: 8.59(5)%). **b**, Schematic representation of the crystal structure. The distorted CoO₄ tetrahedron is emphasized by demonstrating the considerable off-center of the Co atoms. **c**, Rietveld refinement of neutron diffraction data collected at 1.8 K using the magnetic space group $P6_3$. The arrows mark the magnetic reflections.

The structure of BaCoSiO₄ measured by neutron diffraction at 10 K above T_N has the space group $P6_3$, consistent with the reported one from the single crystal X-ray diffraction at room temperature [1]. The Rietveld refinement here adopts the reported crystal structure as a starting structural model [1]. Background was described by linear interpolation of selected points in the pattern. The profile function of the powder time-of-flight neutron diffraction data was described by a convolution of a pseudo-Voigt function with a pair of back-to-back exponential, implemented by the FULLPROF SUITE program. To reduce the number of structural parameters, atoms of the same element were constrained to have the same isotropic displacement parameters. The Rietveld refinement of the neutron diffraction pattern is shown in Fig. S1a and the corresponding structural parameters are tabulated in Table S1. As shown in Fig. S1b, Co²⁺ ions are tetrahedrally coordinated by oxygen forming spin trimers in the ab plane, which are bridged by the adjacent SiO₄ tetrahedra. The spin trimer layer is stacked alternately with the SiO₄ tetrahedra layers along the c axis. The CoO₄ tetrahedron is considerably distorted with a large off-center of Co atoms and one relatively distant (Co-O4) bond ($d_{\text{Co-O4}} = 1.994 \text{ \AA}$) and three smaller bond lengths ($d_{\text{Co-O1}} = 1.946 \text{ \AA}$, $d_{\text{Co-O2}} = 1.944 \text{ \AA}$, $d_{\text{Co-O3}} = 1.938 \text{ \AA}$).

Neutron powder diffraction data collected at 1.8 K using the central wavelength of 2.665 Å were used to determine the magnetic structure without the magnetic field. The magnetic symmetry analysis was performed using the MAXMAGN tool at the Bilbao Crystallographic Server. For a given propagation vector $\mathbf{k} = (1/3, 1/3, 0)$ and the parent grey group $P6_31'$, there are only three \mathbf{k} -maximal magnetic subgroups ($P6_3'$, $P6_3$, $P3$) which were tested by comparing the neutron data at 1.8 K. We found the magnetic space group $P6_3$ (No.173.129) that is compatible with a $\sqrt{3} \times \sqrt{3}$ supercell provides

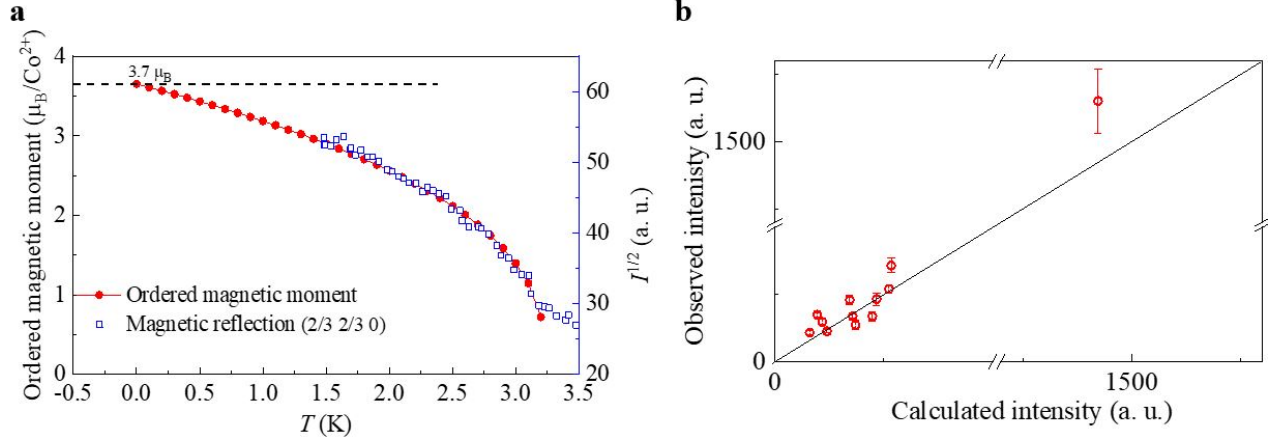


Figure S2: **a**, The square root of the intensity of magnetic reflection (2/3 2/3 0) and the calculated ordered magnetic moment as a function of temperature. **b**, Observed and calculated intensity of the single crystal neutron diffraction at 1.5 K under 2 T.

Table S1: The structure parameters of BaCoSiO_4 measured at 10 K by powder neutron diffraction. The space group is $P6_3$, $a = 9.1124(1)$ Å, $b = 9.1124(1)$ Å, $c = 8.6447(2)$ Å, $\alpha = 90^\circ$, $\beta = 90^\circ$, $\gamma = 120^\circ$. $R_p = 4.62\%$. $R_{\text{Bragg}} = 10.5\%$. The atomic displacement parameter B_{iso} is in $1/(8\pi^2)$ Å².

atom	type	x	y	z	B_{iso}
Ba1	Ba	0	0	0.250	0.23(4)
Ba2	Ba	1/3	2/3	0.224(1)	0.23(4)
Ba3	Ba	2/3	1/3	0.224(1)	0.23(4)
Co1	Co	0.681(1)	0.672(2)	0.529(2)	0.39(5)
Si1	Si	0.6576(9)	-0.0091(8)	0.433(1)	0.39(5)
O1	O	0.7664(7)	0.9146(7)	0.524(1)	0.56(2)
O2	O	0.4648(6)	0.9043(7)	0.489(1)	0.56(2)
O3	O	0.7616(7)	0.1962(7)	0.448(1)	0.56(2)
O4	O	0.7251(5)	0.6542(5)	0.752(1)	0.56(2)

a satisfactory result with the agreement factors $R_p = 5.66\%$ and $R_{\text{Bragg}} = 18.1\%$. The magnetic model as well as the nuclear phase were refined using the FULLPROF SUITE program. The best refinement and the corresponding magnetic configuration are shown in Fig. S1c and Fig. 2d, respectively. The power-law fit of the intensity of magnetic reflection (2/3 2/3 0) (see main text) in the measured temperature range gives a way to extrapolate the intensity at zero temperature. Using the refined magnetic moment at 1.8 K, we can calculate the magnetic moment down to zero temperature. The ordered magnetic moment as a function of temperature is shown in Fig. S2a.

The determination of the magnetic structure under 2 T was done based on the single crystal neutron diffraction data at 1.5 K with the field along the c axis using a similar procedure. Given the propagation vector $\mathbf{k} = \mathbf{0}$ and the parent grey space group, we found two \mathbf{k} -maximal magnetic subgroups: $P6_3'$ and $P6_3$. Due to the symmetry restriction, the former does not support a ferromagnetic component along the c axis, and can thus be excluded. The magnetic space group $P6_3$ is compatible with the neutron diffraction data. Fig. S2b shows the comparison between the observed and calculated neutron diffraction reflections. The best refinement gives the agreement factors $\chi^2 = 16.4$ and $R_F = 10.5\%$. The corresponding schematic drawing of the magnetic structure is shown in Fig. 2e.

S.2 Magnetization characterization

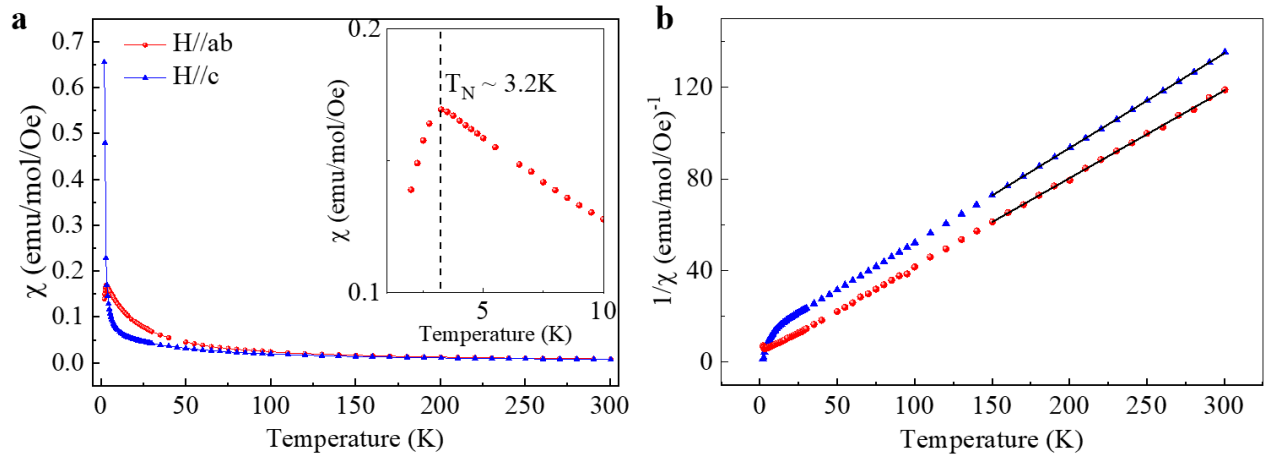


Figure S3: **a**, Temperature dependence of the magnetic susceptibility of BaCoSiO₄ with the magnetic field ($\mu_0 H = 0.1$ T) along the c axis and in the ab plane. Inset shows the magnetic ordering temperature. **b**, Inverse magnetic susceptibility curves and the corresponding fits using the Curie-Weiss law.

S.3 Density functional theory calculations

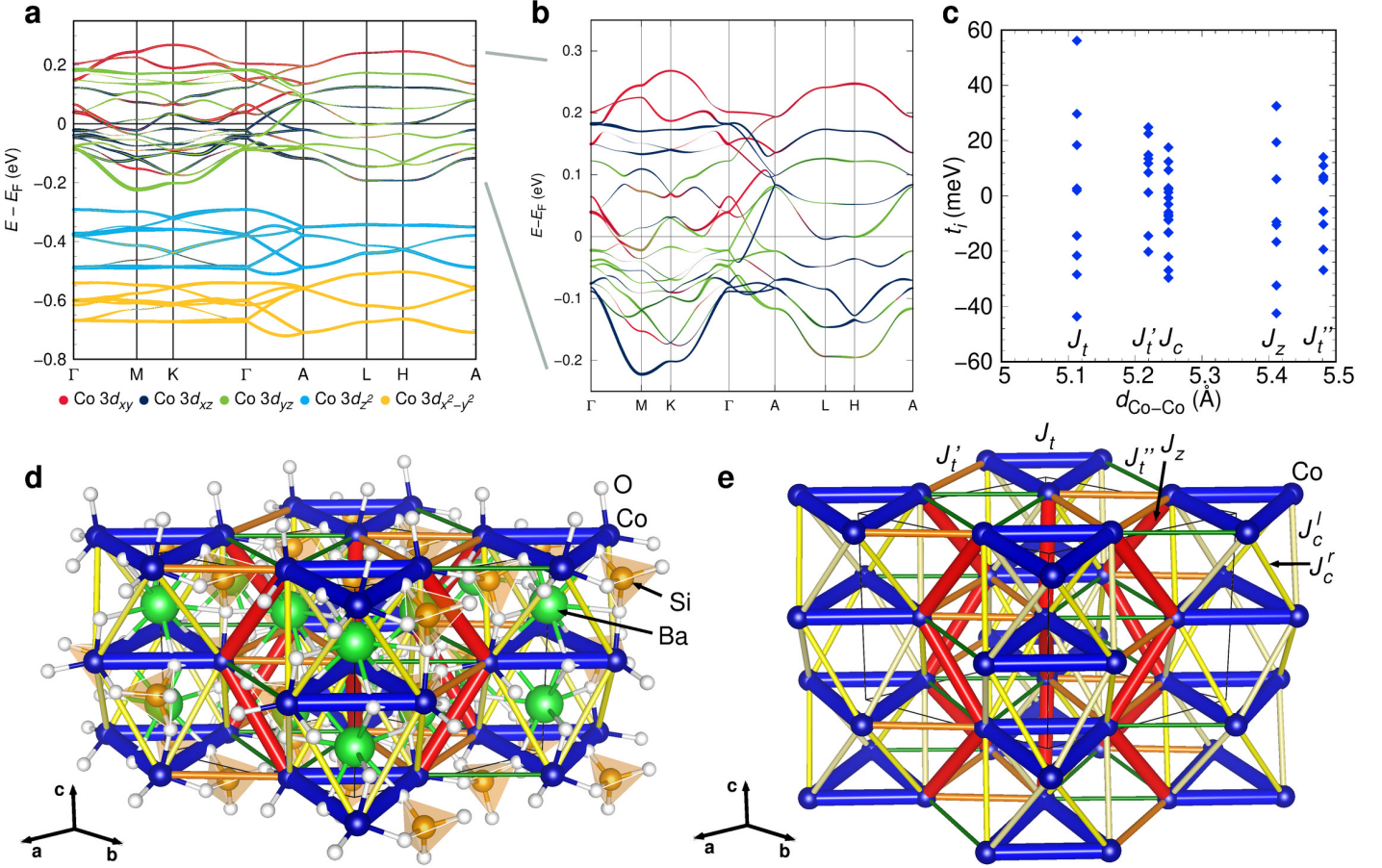


Figure S4: **a** Band structure of BaCoSiO_4 with $3d$ orbital character of one Co highlighted, calculated with FPLO basis and GGA exchange correlation functional. **b** Tight binding fit of the 18 t_{2g} bands in **a**. Bands and orbital character fits the DFT result perfectly. **c** Tight binding parameters of the five nearest Co-Co distances. Labels indicate to which exchange path the t_i contribute. **d** Structure of BaCoSiO_4 with the first five Co-Co exchange paths drawn as bonds. Bond cross section is proportional to exchange coupling strength. **e** Co network with exchange paths as in **d**.

Electronic structure.- We calculated the electronic structure of BaCoSiO_4 using the full potential local orbital (fplo) basis [2] and generalized gradient approximation exchange and correlation functional [3]. Fig. S4 **a** shows the 30 $3d$ bands arising from the six Co^{2+} ions in the unit cell, with $3d$ character of one of the ions highlighted. The local coordinate system is chosen so that the Co-O bonds point into the corners of the cube spanned by the unit vectors. The e_g bands are below the t_{2g} bands and separated from them by a small gap; the t_{2g} bands are half-filled.

Tight binding model.- In order to get an impression which exchange paths might be important, we use projective Wannier functions [4] to obtain a tight binding model for the Co t_{2g} electrons. Bands from this model are shown in Fig. S4 **b** and perfectly match the DFT bands in dispersion and character. Hopping parameters for first five exchange paths are shown in Fig. S4 **c**. These five paths are shown as bonds in Fig. S4 **d** and **e**. In-plane couplings J_t , J'_t and J''_t form triangles; inter-layer couplings J_z define zigzag chains along c , and inter-layer couplings J_c are chiral, with J'_c defining a right screw and J^l_c a left screw; J^r_c and J^l_c belong to the same distance $d_{\text{Co-Co}} = 5.250 \text{ \AA}$ but are symmetry inequivalent. The TB parameters do not rapidly decrease with increasing distance, and the inter-layer hoppings ($d_{\text{Co-Co}} = 5.250 \text{ \AA}$ and 5.411 \AA labeled J_c and J_z) are not substantially smaller than the three in-plane hoppings. On the contrary, there is a suggestion in these parameters that one in-plane coupling (J_t , $d_{\text{Co-Co}} = 5.113 \text{ \AA}$) and one inter-layer coupling (J_z , $d_{\text{Co-Co}} = 5.411 \text{ \AA}$) may play a more prominent role than the other exchange couplings. The conclusion from the tight binding parameters is that it is crucial to calculate all five exchange couplings by energy mapping.

Table S2: Exchange couplings of BaCoSiO₄, calculated for a $\sqrt{2} \times \sqrt{2} \times 1$ unit cell within GGA+U at $J_H = 0.84$ eV and $4 \times 4 \times 4$ k points. The last row contains the Co-Co distances which identify the exchange paths. The errors shown are only the statistical error arising from the energy mapping. The interpolated $U = 4.41$ eV set of couplings (in bold face) reproduces the (average) experimental Curie-Weiss temperature.

U (eV)	J_t (K)	J'_t (K)	J_c (K)	J_z (K)	J''_t (K)	θ_{CW} (K)
3	3.48(1)	0.74(1)	0.50(1)	3.03(1)	0.27(1)	-21.8
3.5	3.11(1)	0.64(1)	0.44(1)	2.64(1)	0.22(1)	-19.2
4	2.80(1)	0.54(1)	0.38(1)	2.32(1)	0.19(1)	-17.0
4.41	2.56(1)	0.49(1)	0.35(1)	2.09(1)	0.16(1)	-15.4
4.5	2.51(1)	0.48(1)	0.35(1)	2.04(1)	0.15(1)	-15.1
d (Å)	5.113	5.220	5.250	5.411	5.481	

Table S3: Exchange couplings of BaCoSiO₄, calculated for a $\sqrt{2} \times 1 \times \sqrt{2}$ unit cell within GGA+U at $J_H = 0.84$ eV and $4 \times 4 \times 4$ k points for the room temperature structure. The last row contains the Co-Co distances which identify the exchange paths. The errors shown are only the statistical error arising from the energy mapping. The interpolated $U = 4.37$ eV set of couplings (in bold face) reproduces the (average) experimental Curie-Weiss temperature.

U (eV)	J_t (K)	J'_t (K)	J'_c (K)	J^l_c (K)	J_z (K)	J''_t (K)	θ_{CW} (K)
3	3.45(2)	0.73(3)	0.46(3)	0.62(3)	3.03(2)	0.28(3)	-21.6
3.5	3.09(2)	0.62(3)	0.40(3)	0.55(3)	2.65(2)	0.24(3)	-19.0
4	2.77(2)	0.54(2)	0.35(2)	0.50(2)	2.32(2)	0.20(2)	-16.8
4.37	2.57(2)	0.49(2)	0.32(2)	0.46(2)	2.11(2)	0.17(2)	-15.4
4.5	2.50(2)	0.47(2)	0.31(2)	0.45(2)	2.04(2)	0.16(2)	-14.9
d (Å)	5.113	5.220	5.250	5.250	5.411	5.481	

Energy mapping. - We now extract the Heisenberg Hamiltonian parameters of BaCoSiO₄ using the energy mapping technique [5]. We use two different supercells: With a $\sqrt{2} \times \sqrt{2} \times 1$ cell for which the results are summarized in Table S2, we can resolve exchange couplings up to $d_{Co-Co} = 9.270$ Å and convince ourselves that only the first five paths shown in Fig. S4 e are relevant. Using a $\sqrt{2} \times 1 \times \sqrt{2}$ supercell, with results reported in Table S3, we are able to separate the left-winding and right-winding chiral couplings J'_c and J^l_c . For the first supercell, the 12 independent Co²⁺ moments in $P1$ symmetry allow for 460 unique energies of different configurations; we randomly choose 39 of these spin configurations and obtain an excellent fit to the Heisenberg Hamiltonian in the form

$$H = \sum_{i < j} J_{ij} \mathbf{S}_i \cdot \mathbf{S}_j \quad (S1)$$

Total moments are exact multiples of $3 \mu_B$ as all Co²⁺ moments are $S = 3/2$. In Table S2, the values of the J_i are given with respect to spin operators of length $S = 3/2$. Please note that if the Hamiltonian is written as \sum_{ij} counting every bond twice, the J_i need to be divided by two. Besides the five couplings shown in Table S2, we find negligibly small longer range couplings $J_6 = 0.01(1)$ K ($d_{Co-Co} = 7.328$ Å), $J_7 = 0.05(1)$ K ($d_{Co-Co} = 7.549$ Å), $J_9 = 0.00(1)$ K ($d_{Co-Co} = 8.963$ Å), $J_{10} = 0.00(1)$ K ($d_{Co-Co} = 9.084$ Å), $J_{11} = 0.03(1)$ K ($d_{Co-Co} = 9.126$ Å), $J_{12} = 0.00(1)$ K ($d_{Co-Co} = 9.237$ Å), $J_{13} = -0.01(1)$ K ($d_{Co-Co} = 9.270$ Å). The Curie-Weiss temperature estimates are obtained from

$$\theta_{CW} = -\frac{2}{3} S(S+1) \left(J_1 + J_2 + 2J_3 + J_4 + J_5 + J_6 + 2J_7 + J_9 + 2J_{10} + 3J_{11} + 2J_{12} + J_{13} \right) \quad (S2)$$

where $S = 3/2$. The U value is determined by demanding that the couplings reproduce the experimental Curie-Weiss temperature. From fits to the inverse susceptibility, we have $\theta_{CW} = -10(2)$ K for $H \parallel ab$ and $\theta_{CW} = -26.2(4)$ K for

$H \parallel c$. As approximate energy scale, we use a weighted average of these two values, $\theta_{\text{CW}} = -15.4$ K. The corresponding interpolated set of exchange couplings is given in Table S2 in bold face.

For the second supercell ($\sqrt{2} \times 1 \times \sqrt{2}$), the 12 independent Co^{2+} moments in $P1$ symmetry lead to 195 spin configurations with distinct energies out of which we use 38 for the energy mapping. Besides the six couplings given in Table S3, we obtained negligibly small $J_8 = 0.05(1)$ K ($d_{\text{Co-Co}} = 8.683$ Å) and $J_{14} = 0.01(1)$ K ($d_{\text{Co-Co}} = 10.076$ Å). The two chiral couplings J_c^r and J_c^l turn out to be substantially different, with J_c^r 50% larger than J_c^l .

Fully relativistic calculations.- We use collinear relativistic DFT calculations to estimate the single ion anisotropy $E_{\text{SIA}} = AS_z^2$. In order to separate E_{SIA} from anisotropic exchange, we calculated total energies for three different spin configurations for the six Co ions in the unit cell: a) FM (ferromagnetic). b) TAFM (one J_t triangle up, one J_t triangle down). c) STRIPY (up-up-down in one J_t triangle, up-down-down in the other). We calculated energies for moments $\mathbf{m} \parallel \mathbf{x}$, $\mathbf{m} \parallel \mathbf{y}$, and $\mathbf{m} \parallel \mathbf{z}$; the first two energies are the same, the third is higher. We use both plain GGA+SO calculations and GGA+SO+U with $U = 4$ eV (the value we know to describe the material correctly). The single ion anisotropy energy estimates are listed in Table S4. The fact that the dependence on spin configuration is small (only about 10% variation) indicates that anisotropic exchange is not strong.

Table S4: Estimates of single ion anisotropy energies A for three spin configurations.

	A_{FM} (K)	A_{TAFM} (K)	A_{STRIPY} (K)
GGA+SO	1.85	1.85	1.82
GGA+SO+U ($U = 4$ eV)	2.38	2.14	

S.4 Theoretical modeling

Consider one triangle with three spins coupled by the DM interactions that respect the 3-fold rotation symmetry. The total energy is given by $E_{\text{DMI}}^{\text{tot}} = (\mathbf{S}_1 \times \mathbf{S}_2) \cdot \mathbf{D}_3 + (\mathbf{S}_2 \times \mathbf{S}_3) \cdot \mathbf{D}_1 + (\mathbf{S}_3 \times \mathbf{S}_1) \cdot \mathbf{D}_2$, where spins $\{\mathbf{S}_i, i = 1, 2, 3\}$ are numbered counterclockwise on the triangle, and \mathbf{D}_i is the DM vector on the opposite edge of \mathbf{S}_i . The energy associated with the out-of-plane component of the DM vectors is $E_{\text{DMI}}^z = D_z \hat{z} \cdot (\mathbf{S}_1 \times \mathbf{S}_2 + \mathbf{S}_2 \times \mathbf{S}_3 + \mathbf{S}_3 \times \mathbf{S}_1) \equiv D_z \hat{z} \cdot \boldsymbol{\epsilon}$, where $\boldsymbol{\epsilon}$ is the vector spin chirality. This term always favors coplanar spin configurations, for which $|\hat{z} \cdot \boldsymbol{\epsilon}|$ is maximized (Fig. S5).

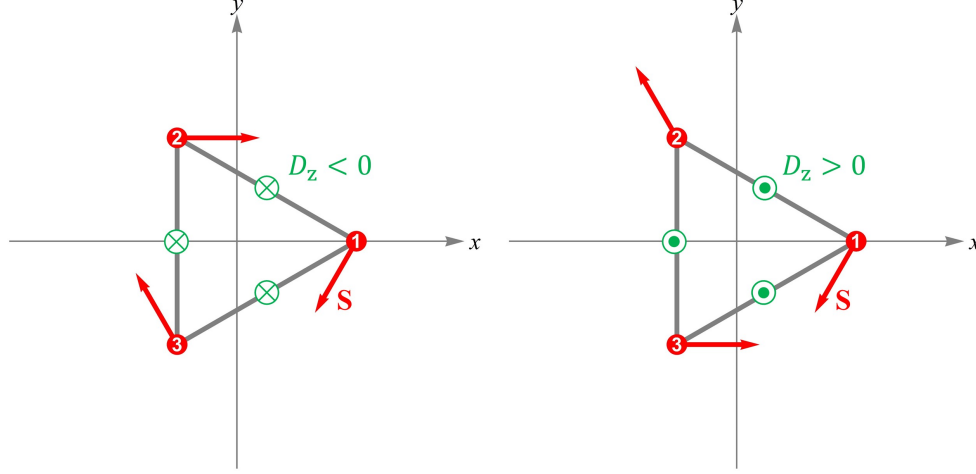


Figure S5: Minimal energy configuration for $D_z < 0$ (Left) and $D_z > 0$ (Right). A uniform rotation applied to all spins does not change energy.

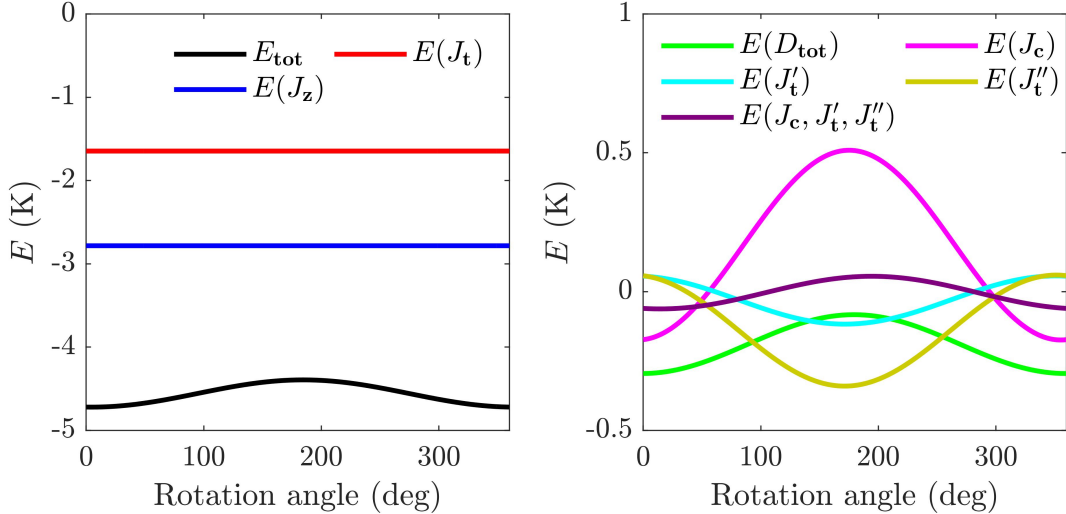


Figure S6: Energy per spin for each of the terms in the Hamiltonian as a function of rotation angle.

Focusing on spin configurations with the 3-fold rotation symmetry, we derive the total DMI energy with a spin and the DM vector on its opposite edge written in the same local frame, $\mathbf{V}_i = V_z \hat{z} + V_\perp (-\hat{\mathbf{r}}_i) + V_\parallel \hat{z} \times (-\hat{\mathbf{r}}_i)$ where $V \equiv S$ or D [Fig. 3a], and $\hat{\mathbf{r}}_i$ is the unit vector from the center of the triangle pointing to site i . The result is

$$E_{\text{DMI}}^{\text{tot}} = \frac{3}{2} \sqrt{3} D_z (S_\parallel^2 + S_\perp^2) + 3 \sqrt{3} S_z (D_\parallel S_\parallel + D_\perp S_\perp) \equiv \frac{3}{2} \sqrt{3} D_z |\mathbf{S}_{xy}|^2 + 3 \sqrt{3} S_z \mathbf{S}_{xy} \cdot \mathbf{D}_{xy}, \quad (\text{S3})$$

where $\mathbf{S}_{xy} = (S_{\perp}, S_{\parallel})$ with the \mathbf{S}_i component parallel to radius-vector \mathbf{r}_i as S_{\parallel} and that perpendicular to it S_{\perp} , and $\mathbf{D}_{xy} = (D_{\perp}, D_{\parallel})$. Other relevant physical quantities can be calculated: toroidal moment $\mathbf{t} = \sum_i \mathbf{r}_i \times \mathbf{S}_i = 3S_{\perp}\hat{\mathbf{z}}$; vector spin chirality $\boldsymbol{\epsilon} = \mathbf{S}_1 \times \mathbf{S}_2 + \mathbf{S}_2 \times \mathbf{S}_3 + \mathbf{S}_3 \times \mathbf{S}_1 = \frac{3\sqrt{3}}{2}S_{xy}^2\hat{\mathbf{z}}$; scalar spin chirality $\kappa = (\mathbf{S}_1 \times \mathbf{S}_2) \cdot \mathbf{S}_3 = |\boldsymbol{\epsilon}|S_z$.

To understand the role played by the subleading interactions, we start with the energy-minimized ferritoroidal structure in zero field, continuously rotate along the c-axis all spins on the sublattice with toroidal moment opposite to the net moment and plot the energy of each term in the Hamiltonian as a function of rotation angle in Fig. S6. The left panel shows the total energy (black), the energy of J_t bonds (red) and that of J_z (blue). Since the global rotation occurs within one of J_t - J_z sublattices, the energy of these two bonds stays the same. The right panel of Fig. S6 shows the energy of all subleading interactions. It is evident that the J_c term favors the ferritoroidal state, while J'_t and J''_t favors the ferrotoroidal one.

References

- [1] Liu, B. & Barbier, J. Structure of the stuffed tridymite derivatives, BaMSiO_4 ($M = \text{Co}, \text{Zn}, \text{Mg}$). *J. Solid State Chem.* **102**, 115–125 (1993).
- [2] Koepnik, K. & Eschrig, H. Full-potential nonorthogonal local-orbital minimum-basis band-structure scheme. *Phys. Rev. B* **59**, 1743–1757 (1999).
- [3] Perdew, J. P., Burke, K. & Ernzerhof, M. Generalized gradient approximation made simple. *Phys. Rev. Lett.* **77**, 3865–3868 (1996).
- [4] Eschrig, H. & Koepnik, K. Tight-binding models for the iron-based superconductors. *Phys. Rev. B* **80**, 104503 (2009).
- [5] Iqbal, Y. *et al.* Signatures of a gearwheel quantum spin liquid in a spin-1/2 pyrochlore molybdate Heisenberg antiferromagnet. *Phys. Rev. Mater.* **1**, 071201(R) (2017).